ZIBELINE INTERNATIONAL™ PUBLISHING

ISSN: 2616-4302 (Online)
CODEN: AMMCFL

Acta Mechanica Malaysia (AMM)

DOI: http://doi.org/10.26480/amm.01.2024.28.39

RESEARCH ARTICLE

DRAG REDUCTION OF A FINITE CIRCULAR CYLINDER WITH A BOXFISH-LIKE EXTENDED SURFACE

Shorob Alam Bhuiyan, Ikram Hossain, Redwan Hossain, Md. Sakib Ibn Mobarak Abir and Dewan Hasan Ahmed*

Department of Mechanical and Production Engineering, Ahsanullah University of Science and Technology, 141-142 Love Road, Tejgaon Industrial Area, Dhaka, Bangladesh.
Corresponding Author Email: dhahmed.mpe@aust.edu

ARTICLE DETAILS

Article History:

Received 20 January 2023
Revised 18 February 2024
Accepted 06 March 2024
Available online 08 March 2024

ABSTRACT

In numerous aerodynamic applications, the greater drag coefficient of the bluff body in transitional flow, i.e., at subcritical Reynolds numbers, is one of the most significant problems.

Current research focuses on the drag reduction of a circular cylinder by utilizing a passive technique, both numerically and experimentally, for the subcritical Reynolds number with a range of 8.85×10^4 to 1.98×10^5. Initially, the frontal shape of the Boxfish was considered an extended surface and had a detrimental effect on drag reduction. Later, a modified design of the frontal part of the Boxfish is considered as an extended surface, and studies are carried out for three stem lengths (distance between the extended surface and cylinder) with a wide range of angles of attack. At an attack angle of 0°, a stem length of 80 mm reduces drag by 71% compared to a cylinder with no stem. Where 33% of the results integrating angle of attack were reduced at 5° angle of attack and 70 mm stem length, Current research suggests that a stem length of 80 mm reduces drag across a broad Reynolds number range. Numerical and experimental data indicate that boundary layer detachment and reattachment, as well as wake generation, decrease drag. Hence, offering a proposed design for future vehicles that generates less drag, thereby reducing environmental pollution.

KEYWORDS

Boxfish, drag reduction, bluff body, extended surface, subcritical Reynolds number.

1. INTRODUCTION

Numerous aerodynamic applications exist for the cylinder's surface including the casing (body) of rockets, the main body of airplanes, the surrounding body of airplane propellers, as well as many automotive parts and athletic equipment. Since the beginning of aerodynamic studies, numerous researchers have been interested in maximizing aerodynamic efficiency by minimizing the drag of cylindrical bodies. In this field of study, numerous experimental and computational experiments have been undertaken (Asif et al., 2016). Researchers have extensively explored both active and passive approaches for reducing the drag force on a circular cylinder (Eun et al., 2018; Zhang et al., 2020). For active method in drag reduction, a group researcher divide active drag reduction methods into four categories: drag reduction based on wall motion; drag reduction based on volume force control; drag reduction based on wall deformation; and drag reduction based on micro-vibration generated by a piezoelectric actuator (Zhang et al., 2020). And some other popular techniques utilize a rotating cylinder, and active sensor (Kerho et al., 2000).

Additionally, semi-conical piers can be up to 46% more effective than cylindrical piers (Aghaee-Shalmani and Hakimzadeh, 2022). When birds flap their wings to reduce drag, found that tiny flaps reduce drag by 73% while continuous flaps reduce drag by 66% (Asif et al., 2016). Thus, the major benefit of active methods is more flexibility for a wide range of applications without body shape modification (Sudin et al., 2014). On the other hand, passive techniques gained more attention from researchers than overactive techniques as there is no external power required. A group researcher discovered that the addition of a spoiler and a slice diffuser to a KIA PRIDE automobile model reduced drag (Saleh et al., 2020). Furthermore, riblets, dimples, oscillating walls, compliant surfaces, helical wire, microbubbles, and even the addition of a channel through a circular cylinder are alternative methods of drag reduction which can reduce drag up to 50% (Savill, 1990; Abdulbari et al., 2013; Ahmed et al., 2017; Haidary et al., 2020; Bearman and Harvey, 2012).

According to research, a circular cylinder in the upstream position will reduce the drag of the downstream circular cylinder. Igarashi and Zdravkovich classified the wake flow of tandem configurations as extended body regime, reattachment zone, and co-shedding zone (Igarashi, 1981; Zdravkovich, 1990). To better understand the reattachment, Xu and Zhou divided it into two sub-regimes, one of which takes place upstream of the downstream cylinder and the other downstream (Xu and Zhou, 2004). The wake structures of tandem circular cylinders were studied by numerous researchers (Wu et al., 1994; Lin et al., 2002; Alam et al., 2018; Carmo et al., 2010; Alam and Zhou, 2008). They classified different flow configurations based on the separation between the upstream and downstream cylinders.

In addition, further research indicates that an upstream rod can lessen the resistance of a downstream cylinder. A group researcher discovered that an upstream rod can lower the drag of a downstream cylinder at various distances between the rod and the cylinder, with a maximum drag reduction of 2.34% compared to a single cylinder (Wang et al., 2018). Some researchers discovered that the upstream rod can lower the mean drag and lift fluctuation of the cylinder, particularly in the cavity flow mode with the rod diameters ranging from d/D = 0.3 and 0.5 (Zhang et al., 2006). Tsutsui and Igarashi determined that the optimal circumstances for drag reduction are d/D = 0.25, and L/D = 1.75–2.0 (Tsutsui and Igarashi,

Quick Response Code	Access this article online	
	Website: www.actamechanicamalaysia.com	DOI: 10.26480/amm.01.2024.28.39

Cite the Article: Shorob Alam Bhuiyan, Ikram Hossain, Redwan Hossain, Md. Sakib Ibn Mobarak Abir and Dewan Hasan Ahmed (2024). Drag Reduction of A Finite Circular Cylinder with A Boxfish-Like Extended Surface. *Acta Mechanica Malaysia, 7(1): 28-39.*

2002). In these circumstances, the shear layer from the rod attaches to the front face of the circular cylinder, and vortices do not separate from the rod. These findings suggest that an upstream rod can reduce a downstream cylinder's resistance. Prasad and Williamson minimized drag by 38% by positioning a flat plate perpendicular to the flow and 1.5 diameters upstream of the test cylinder (Prasad and Williamson, 1997).

In addition, altering the upstream bluff body to a T-shaped plate, C-shaped, or equilateral triangular wedge had a similar positive effect on lowering drag (Han et al., 2019; Law and Jaiman, 2017; Alam et al., 2006). Experimental research by Shoshe *et al.* (2021) on five different cylinder diameters and five different stem lengths showed that extended surfaces with finite cylinders positioned at specific intervals could reduce pressure-induced drag by as much as 60%. Additionally, moving the extended surface 66% upstream of the primary cylinder and changing its geometry to a half-C shape resulted in a 55% reduction in drag (Islam et al., 2023).

Siddiqui and Agelin-Chaab suggest that there are several intriguing topics for future research regarding the manipulation of bluff body flow, including the use of passive devices inspired by nature (Siddiqui and Agelin-Chaab, 2021). Numerous researchers have sought to lower drag using various bio-inspired methods, with shark riblets being the most prominent since they delay boundary layer separation, resulting in a 7.59% drag reduction (Ghosh, 2021). A review study on fishes (Nekton), birds (avian), and fast-running land animals as sources of inspiration for drag reduction; each of these species has unique characteristics (Siddiqui and Agelin-Chaab, 2021; Cheney et al., 2021). The Boxfish shape is more structurally and dynamically efficient than the current design model and can be modified to minimize drag and enhance energy economy in motor vehicles (Kozlov et al., 2015).

Computational fluid dynamics (CFD) modeling is popular and inexpensive today for acquiring a better grasp of the variations in coefficients of drag and identifying methods to reduce drag. Nethercot demonstrated that integrating numerical and experimental methodologies leads to increased comprehension (Nethercot, 2002). Numerical approaches can be utilized to address specific problems in experimental mechanics, and this can save time and effort as well as lead to an immense reduction of data (Oanta et al., 2020; Liess and Ilgevičius, 2003). Moreover, Computational fluid dynamics (CFD) can effectively anticipate the wind pressure load between tandem buildings or buildings with complex shapes (Gnatowska, 2019; Korycki et al., 2016). Numerous researchers evaluate *2D* and *3D* simulations as well as different solvers, such as ANSYS CFX 13.0 and OpenFOAM, to identify the optimal numerical approach that requires less computational time and is accurate in experiments (García and Vakkilainen, 2019; Sowoud et al., 2020; Nazari et al., 2018; Stringer et al., 2014).

1.1 Physical Model

Upstream extended surface and bio-inspired drag reduction strategies serve as the motivating factors behind this research. Furthermore, to remain competitive and economically viable, automakers are compelled to produce fuel-efficient vehicles due to rising gasoline costs. Reducing aerodynamic drag is one way for building fuel-efficient automobiles, as it accounts for around 80% of total drag at vehicle cruising speeds greater than 80 kilometers per hour (Hucho and Sovran, 1993). Reducing drag decreases both fuel usage and CO_2 emissions. Over the past four decades, significant drag reductions have been achieved by refining the exterior body shapes of vehicles. In the 1960s and 1970s, the traditional box-shaped passenger cars of the 1920s started to become more aerodynamic as aerodynamics became the primary factor in reducing fuel consumption, especially during the 1973–1974 OPEC oil embargo (Kozlov et al., 2015). It is feasible to minimize the drag coefficient by employing a smooth underbody, intelligent wheels, reduced wheel wells, and convoy driving (platooning).

However, the smooth underbody, wheels, and wheel arches reduce the cooling performance of the car. Therefore, it is essential to develop an alternate body shape with a lower drag coefficient. The Boxfish has a lower aerodynamic resistance than dolphins and penguins, despite its terrible appearance. Due to its huge cross-section and structural robustness, the Boxfish is a better model for automotive body forms. Some automakers, particularly Daimler-Chrysler, are aiming to incorporate the shape of the Boxfish into their vehicle designs (Kozlov et al., 2015). On the aerodynamics of Boxfish, however, little information is currently available in the public domain. Consequently, the primary purpose of this work is to examine the aerodynamic behavior of a Boxfish, particularly the upper frontal portion used as an extended surface using both experimental and computational methods. Using flow visualization, boundary layer separation, and vortex generation behind the extended surface and circular cylinder are the major concerns.

In the beginning, a subsonic wind tunnel was used to calculate the bare cylinder's drag coefficient. In subsequent trials, stem length was varied on the extended surface based on the frontal section of the Boxfish for different flow conditions. ANSYS 2021 R1 was utilized for numerical simulation, and the bare cylinder was subjected to numerical simulation with complete validation and verification based on the literature. Three distinct stem lengths (i.e., upstream locations) of 80 mm, 70 mm, and 60 mm were utilized in 15 cases for experiments and 18 cases for simulations with the extended surface. This simulation investigation proceeded with several Reynolds numbers, including 8.85×10^4, 1.53×10^5, and 1.98×10^5. All simulations were subsequently compared to extended surface model experiments.

2. Experimental Study

2.1 Extended Surface Boxfish

SOLIDWORKS 2020 R1 was utilized for the extended surface design of the selected models. For the model's dimensions, the essential measures were completed, such as utilizing the Tracker analysis program. The measurements are the Boxfish body from the frontal portion to the tail at 450 mm, and this length was used as a reference to measure the other necessary perimeters, such as the frontal shape and a circle diameter covering the middle portion of the Boxfish. The model is produced by a 3D printer when all essential designs have been completed and the boxfish model covers 14.44% of the wind tunnel's test section where the drag is measured accordingly.

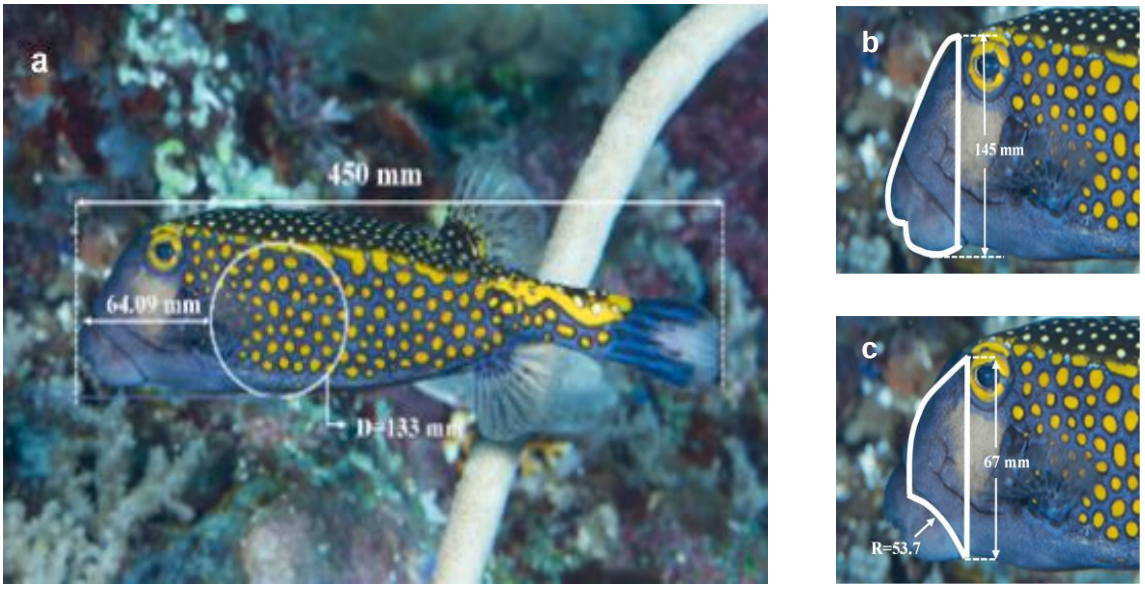

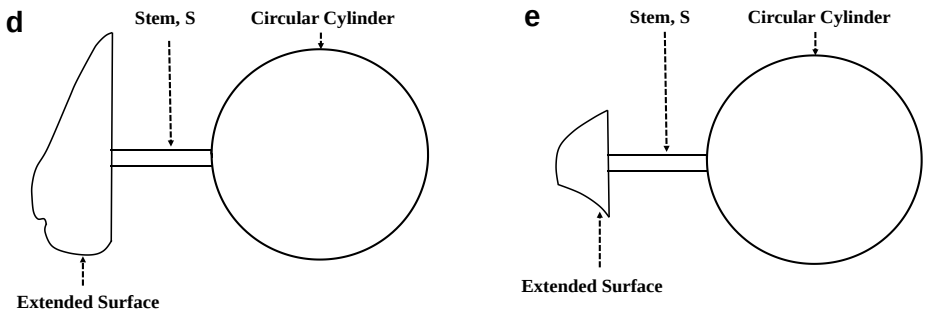

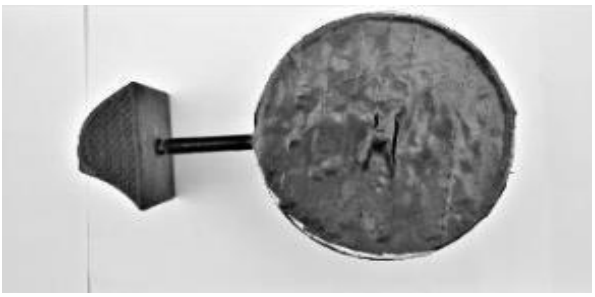

Figure 1: (a) Boxfish measurement; **(b)** Initial design of extended surface; **(c)** Final design of extended surface; **(d)** Schematic diagram of the initial extended surface with a circular cylinder; **(e)** Schematic diagram of the final extended surface with a circular cylinder and **(f)** Fabrications of the extended surface mode

The body form measurement is depicted in Figure 1a, where the circle in the middle has a diameter of 133 mm and the distance from the frontal portion to the circle is approximately 64.09 mm. The extended surface was initially designed as shown in Figure 1b, but the results of the numerical analysis performed at both low and high Reynolds numbers were not as anticipated. As opposed to diminishing, the coefficient of drag rose. This is due to the fact that the initial extended surface illustrated in Figure 1b has a measured vertical height of 145 mm, causing the initial extended surface to cover 109% of the cylinder. The primary objective of this research, however, is to lower the cylinder's drag. Consequently, changes were required to attain the intended result.

Initially, the surface area of the extended surface is lowered by approximately 50%, resulting in a vertical height of 67 mm as depicted in Figure 1c. Furthermore, for each of the 23 species of Boxfish in the world the lip or mouth portion varies (Matsuura, 2015; Alderton, 1967). In addition, the lips are not aerodynamic which has a negative effect. To improve the effectiveness of the streamline, the lip portion is removed and given a radius of curvature of 53.7 mm as shown in Figures 1c, d, and e. Furthermore, the upper portion of the extended surface is curved more toward the cylinder. The observed diameter and distance are utilized to determine the diameter of the circular cylinder and stem length depicted in Fig. 1d, and Fig. 1e shows the fabrication of the extended surface model. Three of the identified stem lengths and three potential stem lengths were investigated: 80 mm, 70 mm, and 60 mm, respectively.

2.2 Test section

TecQuipment's AF100 subsonic wind tunnel was used for the investigation. The test portion of the wind tunnel was 600 mm long with a cross-section of 305 mm × 305 mm and an air velocity working range of 0 to 36 m/s. All the necessary information of the wind tunnel were collected from literature such as where the standard deviation of the mean velocity in the wind tunnel is less than 1%, and the RMS value is less than 0.03% (Shoshe et al., 2021; Asif et al., 2016; Haidary et al., 2020). In the test section, a typical pitot-static tube and a digital DT-8920 manometer with an accuracy of 0.3% and 0.2% repeatability were employed to measure dynamic pressure.

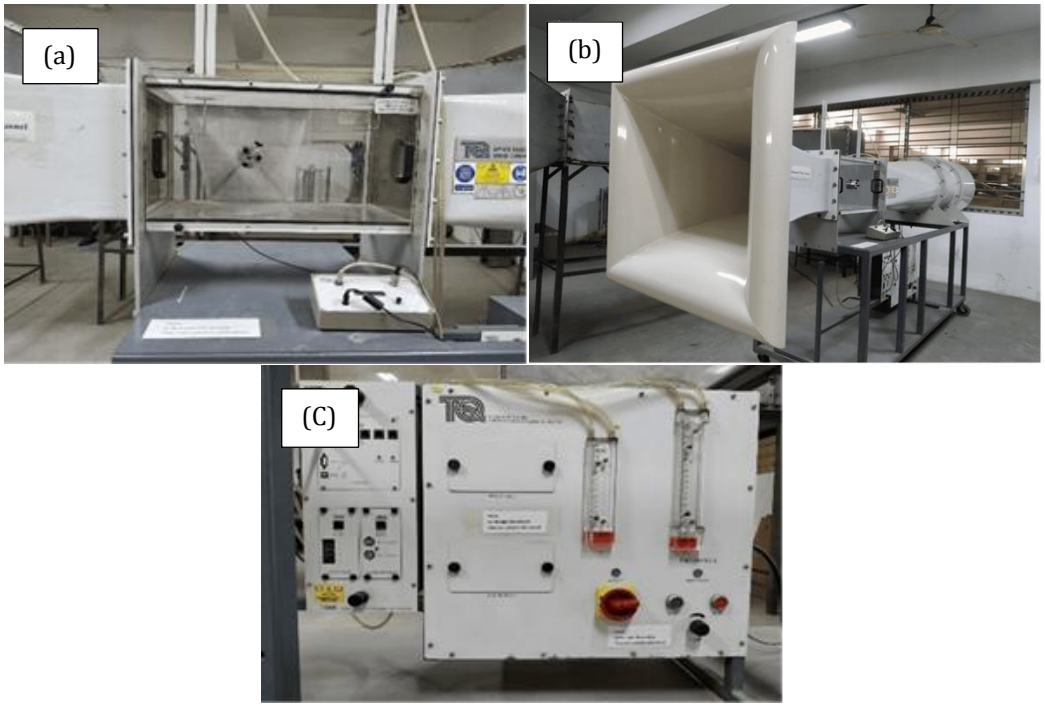

Figure 2: Experimental setup (**a**) AFA2-Balance Assembly, (**b**) AF100 subsonic wind tunnel, (**c**) Digital display of AFA2 and DT-8920 digital manometer

2.3 Measurement of drag force

AFA2-Balance Assembly was utilized for measuring the drag force. The dummy communicates the force exerted on the model to the strain gauge load cell of the AFA2-Balance Assembly, and the immediate digital display of the load cell shows the readings. A second dummy arm is placed on the opposite side of the circular model for symmetry.

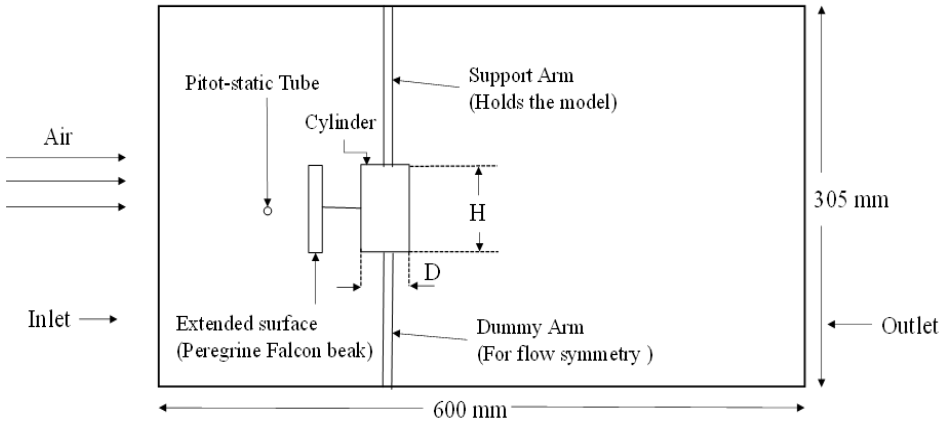

Figure 3: Schematic diagram of the test section with the extended surface model top view

In Figure 3, D represents an 85 mm cylinder and H represents the cylinder's height along its extended surface with is 101 mm. To obtain the necessary drag force from the model, the force on the dummy arm (F_{arm}) is first measured, followed by force on the model with the dummy arms ($F_{measured}$). By subtracting F_{arm} from $F_{measured}$, the needed drag force for a cylinder without an expanded surface (F_{bare}) or with an extended surface ($F_{modified}$) can be determined.

$$F_{\text{modified}} = F_{measured} - F_{arm} \quad (1)$$

$$F_{bare} = F_{measured} - F_{arm} \quad (2)$$

The computed drag force is then compared to the drag coefficient formul a.

$$C_{D_b} = \frac{2F_{bare}}{\rho U^2 A} \quad (3)$$

$$C_{D_b} = \frac{2F_{modified}}{\rho U^2 A} \quad (4)$$

Thus, in Eq. (3) and (4), 'A' represents the reference area, and it represen ts the product of the height (H) and diameter (D).

2.4 Uncertainty Analysis

A necessity for experimentation is uncertainty analysis. For each model, the standard deviation (*SD*), standard error (*SE*), and relative standard deviation (*RSD*) are calculated to determine uncertainty (Holman, 2011).

$$SD = \sqrt{\frac{\sum_1^N (X_i - X_n)^2}{N}} \quad (5)$$

$$SE = \frac{SD}{\sqrt{N}} \quad (6)$$

$$RSD = \frac{SD}{X_n} \quad (7)$$

Here,

$X_i = Value$

$X_n = Mean$

$N = Number\ of\ values$

For determining the standard deviation, multiple procedures were performed for each model using a variety of drag force collection methods. In the wind tunnel, the drag force was altered by adjusting the pressure head. As the drag force changes in the wind tunnel, the data were initially examined for two minutes and then recorded every ten seconds. Again, regardless of time, the drag force was measured by increasing the pressure head and then decreasing the pressure head. Standard deviation (*SD*), Standard error (*SE*), and relative standard deviation were determined following the collection of multiple values for each variable. The greatest standard error is 0.04, and the standard deviation is less than 5%. For determining the coefficient of drag's uncertainty, the uncertainties of the product function are utilized. Eq. (8) is,

$$\omega_R = \sqrt{\sum (\frac{\partial R}{\partial X_i} \times \omega_{X_i})^2} \quad (8)$$

Where the ω_R represents the uncertainty of the result R and ω_{X_i}. Which is the uncertainty of the independent variable X_i. For the rest of the cases and models, the uncertainty is done in the same way (Holman, 2011).

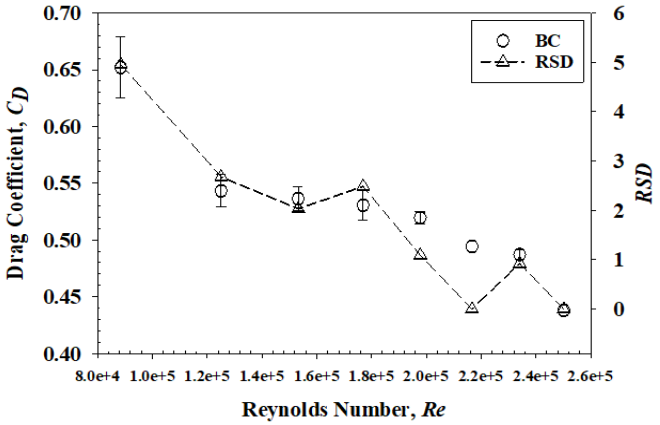

Figure 4: Average drag coefficient values with respective standard error (*SE*) and relative standard deviation (*RSD*) for bare cylinder (BC) in a range of Reynolds numbers

On the right y-axis of Figure 4 is the relative standard deviation (RSD), and on the left y-axis is the drag coefficient. At a low Reynolds number, *Re* = 8.85×10^4, the *SD*, *SE*, and *RSD* were high, with values of 0.03, 0.03, and 4.9%, respectively. Reynolds number grows, *RSD* drops and experiments are conducted at lower *RSD* ranges, suggesting less uncertainty, and increasing the acceptability of this study's examination.

3. Numerical Study

3.1 Mathematical model

As part of an exhaustive investigation into the reduction of drag in the subcritical Reynolds number zone, numerical calculations are conducted. For the conservation mass, the continuity equation is used. As the physical principle states, there is no way to produce or destroy mass. Whenever this notion is simulated for a finite control volume V and a fixed surface area S in space, the concept is known as the finite control volume method. The equation can be presented as,

$$\frac{\partial}{\partial t} \iiint_v \rho\, dV + \iint_s \rho V \cdot ds = 0 \quad (9)$$

In Eq. (9), the first integral over the control volume V represents the temporal rate of change of mass within the control volume, and the second integral represents the net flux of mass out of the control volume via the control surface (Anderson, 2011).

Newton's second law is the second fundamental concept upon which

theoretical dynamics is based. The physical premise is "Force = Rate of Momentum Change Over Time." When this fundamental principle is applied to a fixed, finite control volume, we have.

$$\frac{\partial}{\partial t}\iiint_v \rho V\ dV + \oiint_s (\rho V \cdot ds) = -\oiint_s P\ ds + \iiint_v \rho f\ dv + Fviscous \qquad (10)$$

The left side of Eq. (10) is the first integral. The second is the control volume's net change in momentum through the control surface. On the right hand is the sum of the total force as it flows through the fixed control volume, with the first integral representing pressure force, the second integral representing body force, and the third integral representing the overall viscous force. The momentum equation can also be classified by fluid viscosity. The momentum equation for inviscid flow (F_{viscous} = 0) is known as the Euler equation. The equation for viscous flow is also known as the Navier-Stokes equation (Anderson, 2011).

For the numerical simulation, the SST k- ω transition model was employed. The Transition SST k- ω model is used to represent turbulent flows where the boundary layer is predominantly laminar. This model is additionally referred to as the γ- Re_θ a model since it utilizes γ and Re_θ equations in addition to the k and ω equations of the SST. To complete the model for γ- Re_θ, three correlations are required: $Re_{\theta t}$, $Re_{\theta c}$ and F_{length}. A group researchers initially presented the association between $Re_{\theta t}$, the momentum thickness Reynolds number at which skin friction begins to increase, and $Re_{\theta c}$, the momentum thickness Reynolds number at which intermittency first begins to increase (Menter et al., 2006). The model's closure depends on expressions for $Re_{\theta c}$ and F_{length} as functions of the transferred transition momentum thickness Reynolds number ($\tilde{R}e_{\theta t}$). For plausible correlation of these forms, both physical intuition and numerical experiments were done (Malan et al., 2022). Where they reasoned that, by design, $\tilde{R}e_{\theta t}$= $Re_{\theta t}$ in the freestream. The transport equations are a subset of the SST k- ω model as reported Menter, with a minor change and the addition of two additional transport equations for the usage of γ and Re_θ. (Menter, 1993).

For the turbulent kinetic energy k,

$$\rho\frac{D(k)}{Dt} = \frac{\partial}{\partial x_j}\left[(\mu + \sigma_\kappa \mu_t)\frac{\partial \kappa}{\partial x_j}\right] + \left(\gamma_{eff}\mu_t S^2 - \rho\kappa\frac{\partial u_j}{\partial x_j}\right) - \min\left[\max\left(\gamma_{eff}, 0.1\right), 1\right]\rho\beta^*[1 + F(M_t)](\omega\kappa - \omega_0\kappa_0) \qquad (11)$$

For the specific dissipation rate ω,

$$\rho\frac{D(\omega)}{Dt} = \frac{\partial}{\partial x_j}\left[(\mu + \sigma_\omega \mu_t)\frac{\partial \omega}{\partial x_j}\right] + \alpha\left(\mu_t S^2 - \rho\kappa\frac{\partial u_j}{\partial x_j}\right) - \rho\beta(\omega^2 - {\omega_0}^2) + 2\rho(1 - F_1)\sigma_{\omega^2}\frac{1}{\omega}\frac{\delta y}{\delta x_j}\frac{\delta \omega}{\delta x_j} \qquad (12)$$

S and γ_{eff} is the strain rate tensor modulus, and the effective intermittency, according to the preceding equation. The ambient turbulence values are defined as k and ω_0 are employed as source terms to inhibit turbulence decay. Function F expresses dilatation-dispersive incompressible flow. Here ρ depicts the density, u_j represents the velocity vector, μ represents the molecular viscosity, μ_t and F_1 represents the eddy viscosity and a function accordingly (Malan et al., 2022). Two transport equations make up the γ- Re_θ transition model.

For the intermittency γ,

$$\rho\frac{D\gamma}{Dt} = \frac{\partial}{\partial x_j}\left[\left(\mu + \frac{\mu_t}{\sigma_\gamma}\right)\frac{\partial \gamma}{\partial x_j}\right] + F_{\text{length}}\, c_{a1}\rho S(\gamma F_{\text{onset}})^{0.5}(1 - c_{e1}\gamma) + c_{a2}\rho\Omega\gamma F_{\text{turb}}\,(1 - c_{e2}\gamma) \qquad (13)$$

For transported transition momentum thickness Reynolds number $\tilde{R}e_{\theta t}$,

$$\rho\frac{D\tilde{R}e_{\theta t}}{Dt} = \frac{\partial}{\partial x_j}\left[\sigma_{\theta t}(\mu + \mu_t)\frac{\partial \tilde{R}e_{\theta t}}{\partial x_j}\right] + c_{\theta t}\frac{(\rho U)^2}{500\mu}\left(Re_{\theta t} - \tilde{R}e_{\theta t}\right)(1 - F_{\theta t}) \qquad (14)$$

The magnitude of the local velocity and the modulus of the vorticity tensor are denoted by U and, Ω respectively. The duration and location of the transition's onset respectively represented by the parameters F_{lenght} and F_{onset} govern. F_{turb} and $F_{\theta t}$ are the parameters for regulating the boundary layer breakdown and the boundary layer detector, respectively. Neumann (zero-flux) wall boundary conditions are applied to γ and $Re_{\theta t}$. Initially, γ =1.0 and $\tilde{R}e_{\theta t}$ is calculated utilizing the freestream correlation for $Re_{\theta t}$ as mentioned before (Menter et al., 2006).

3.2 Geometry and Meshing

In numerical research, the diameter and height of the bare cylinder was assumed to be 133 mm and 101 mm, and the remainder of the fluid domain was chosen appropriately, as depicted in Figure 3.

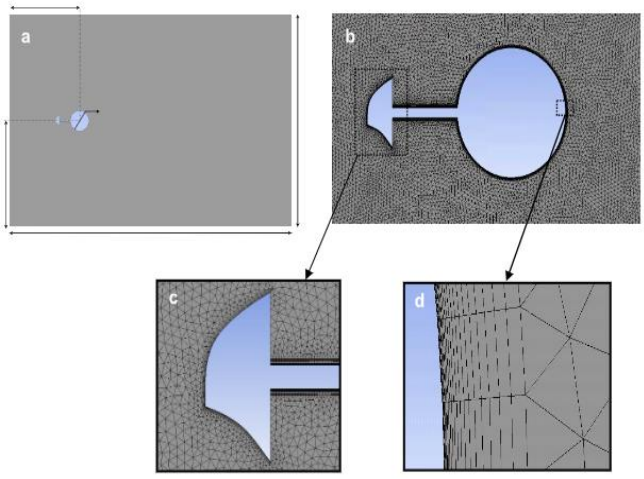

Figure 5: (**a)** Extended surface with the cylinder in the fluid domain; (**b)** Meshing of the domain; (**c)** Zoom view of the extended surface mesh; (**d)** Zoom view of the mesh

As seen in Figures 5c and 5d, the mesh for both the extended surface and cylinder was an unstructured mesh with inflation. In the simulation investigation, the subcritical Reynolds number was y^+ = 1. y^+ represents an arbitrary distance between the first boundary layer and the nonslip wall.

3.3 Boundary conditions and solution control

Using four distinct Reynolds numbers, the entrance velocity for uniform flow is computed for cylinder research. Calculated as the inlet velocity for the subcritical Reynolds number. As the selected Reynolds number transitions from laminar to turbulent, the Transition SST k-ω model was applied to the computation by the flow solver. The 'Coupled Algorithm' was chosen for coupling pressure and velocity from the available algorithms. The simulations lasted approximately ten seconds, and the intensity of the turbulent flow reflected wind tunnel conditions.

3.4 Grid Independence Test

A test of grid independence was conducted to determine the optimal grid size. For proper boundary layer separation, the grid size must be optimized. Beginning with a simulation at Re = 1×10⁴, the number of nodes or element size was steadily raised to enhance the mesh. As illustrated in Figure 6, as the number of nodes increases, the drag coefficient decreases to a point where it is almost constant.

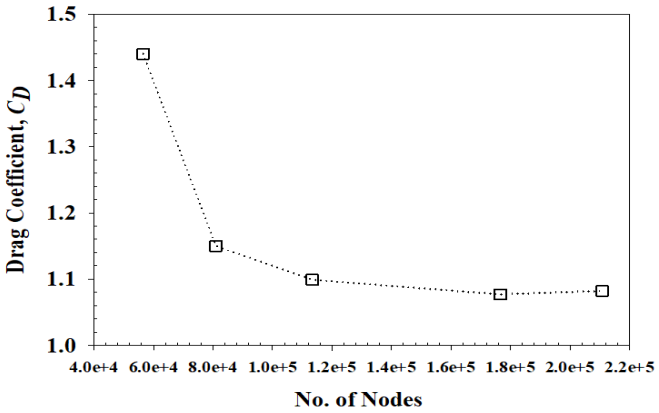

Figure 6: Drag Coefficient, C_D for the bare cylinder variation with the increase of the node numbers

For the simulation analysis, node number 176539 is considered, as its C_D = 1.07 is nearly identical to that of node number 210821, and most significantly, it requires less computational time than higher nodes. The correct mesh characteristics were found using the grid independence test, and numerical simulations for Reynolds numbers between 8.85×10⁴ to 1.98×10⁵ were carried out using the same mesh properties.

3.5 Verification and Validation

A group researcher experiments on a smooth cylinder were compared to those on a bare circular cylinder for the purposes of verification and validation (Munson et al., 1998). Moreover, the simulated result of the

bare cylinder drag coefficient, C_D was compared with other simulated literature such as (Stringer *et al.*, 2014; Rosetti *et al.*, 2012; Yuce and Kareem, 2016). On the other hand, compared the experimental results. All literature comparisons are displayed in Figure 7 (Hoener, 1965; Achenbach, 1971; Hojo, 2015; Zdravkovich, 1990). There are reported inconsistencies between models and experiments, particularly for Reynolds numbers between 8.85×10^4 to 1.98×10^5, which represent the transition from laminar to turbulent flow. This region generates a laminar separation bubble because of boundary layer separation occurring in an erratic manner, resulting in numerous inconsistencies (Selig, 2003). Therefore, these bubbles result in a significant deviation from the simulated outcome. In addition, the simulations were run in *2D* because these results are unable to depict the true three-dimensional nature of the object. However, more processing power and a more precise mesh may produce superior outcomes.

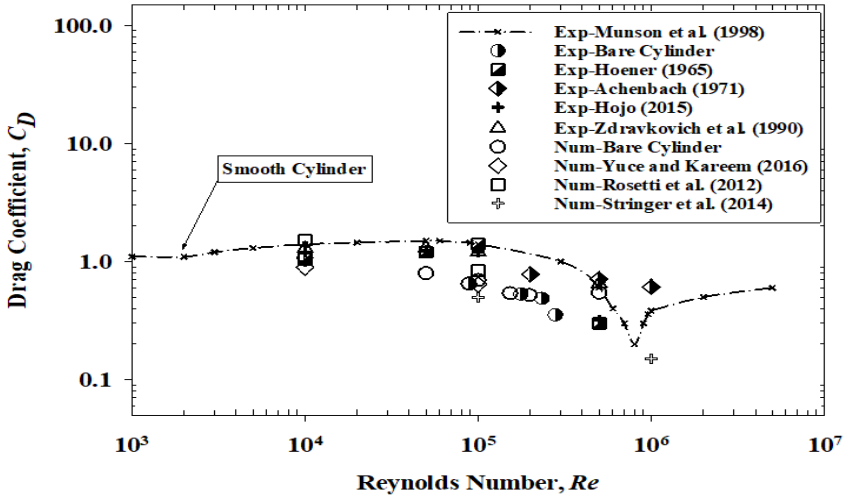

Figure 7: Comparison of bare cylinder drag coefficient with numerical and experimental results for different Reynolds numbers

4. Results and Discussions

4.1 Experimental Results on extended surface model

Further experimental research is conducted with the extended surface, which is considered to be the frontal section of the Boxfish. Experiments are conducted on 15 cases with a constant cylinder diameter and three variable stem lengths (60 mm, 70 mm, and 80 mm) and five different angles of attack (0°, 5°, 10°, 15°, and -10°) for each stem length. All the cases are carried out for on the Reynolds numbers ranging from 8.85×10^4 to 1.98×10^5. In the notation S80A0, 'S' represents a stem length of 80 mm, and 'A' indicates an angle of attack of 0° with a constant diameter of 133 mm for all cases.

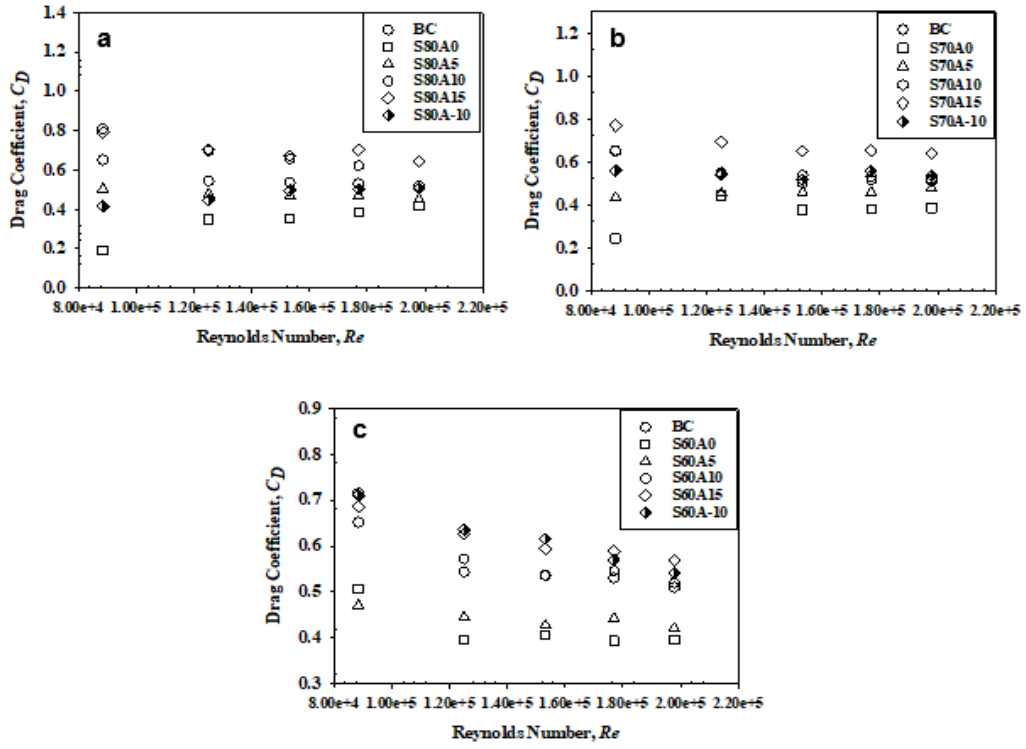

Figure 8: Extended surface model at different AOA for stem length, (**a)** 80 mm; (**b)** 70 mm; and (**c)** 60 mm

Figure 8 displays the drag coefficient for three distinct stem lengths and a wide variety of attack angles for various Reynolds numbers. With a low Reynolds number, the drag coefficient is high for each stem length because of laminar separation bubbles. This bubble causes vortices to form behind the stretched surface, hence increasing drag. In addition, Figure 8 indicates that the drag coefficient is highly dependent on stem length, attack angle, and *Re*. For a low Reynolds number, a longer stem length with a lower angle of attack results in a lower drag coefficient (C_D), but for a high Reynolds number, a shorter stem length with a greater angle of attack results in a lower drag coefficient. In conclusion, the drag coefficient is affected by stem length, angle of attack, and cylinder diameter (Shoshe et al., 2021).

4.2 Drag Reduction Percentile

As demonstrated in Figure 10, the Boxfish model has the lowest drag coefficient at 0° angle of attack, which is the direction of fluid flow, when compared to all other cases.

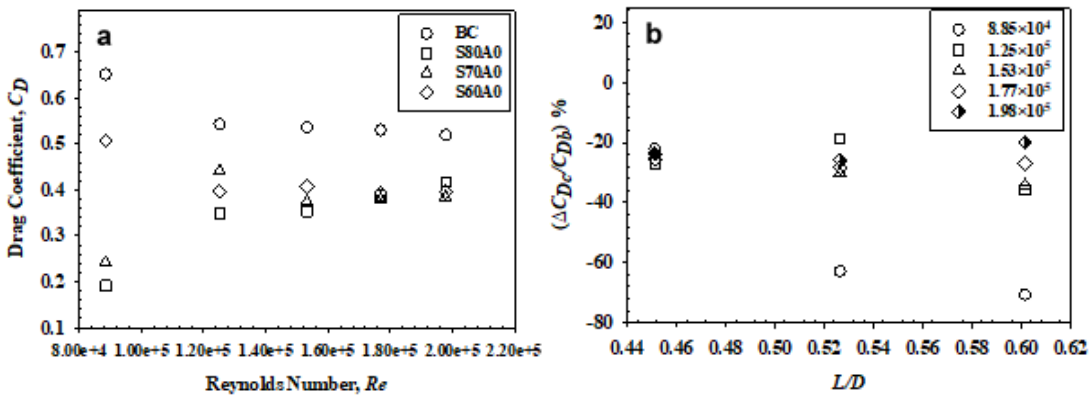

Figure 10: At AOA = 0° (**a)** comparison of different stem lengths and (**b)** drag modification percentile for various Reynolds numbers in the function of L/D ratio

According to Figure 10a, the drag coefficient decreases for all cases compared to the bare cylinder (BC). At a Reynolds number of only 8.85×10^4, the 80 mm stem has the lowest drag coefficient, C_D = 0.20 of the three stem lengths at an attack angle of 0°. The extended surface with a stem length of 70 mm has the lowest drag at 0.38 for a high Reynolds number of 1.98×10^5. On the other hand, to evaluate the drag reduction by adding an extended surface to a bare cylinder, the proportion of drag coefficient reduction of the arrangement (i.e., with the extended surface) is calculated as $\left(\frac{\Delta C_{DC}}{C_{Db}}\right)$ in which C_{Dc} is the drag coefficient of the configuration due to extended surfaces and C_{Db} is the bare cylinder drag coefficient. As illustrated below,

$$\left(\frac{\Delta C_{DC}}{C_{Db}}\right) = \frac{C_{Dc}-C_{Db}}{C_{Db}} \times 100\% \quad (15)$$

In addition, L/D is introduced to indicate the stem length effect on the diameter of the test cylinder as the Reynolds number changes. In Figure 10b, it can be shown that at low stem length for L/D =0.45 ratio, most Reynolds numbers have a similar decrease in drag, while Reynolds number 1.25×10^5 has the greatest reduction in drag by approximately 27%. And when the stem length increases, so do the L/D ratio, and for L/D = 0.53, the greatest decrease occurs at low Reynolds numbers, where 8.85×10^4 achieves the greatest reduction of 63%. At the maximum stem length for L/D = 0.60, the greatest decrease in drag is still attained with 8.85×10^5, at approximately 70%. Hence, as the L/D ratio rises, the most desired outcomes are achieved at low Reynolds numbers.

For further investigation of which stem length is appropriate Figure 11 is plotted. It depicts drag modification percentile $\left(\frac{\Delta C_{DC}}{C_{Db}}\right)$ with changing Reynolds number starting from low Reynolds number 8.85×10^4 to high Reynolds number 1.98×10^5 and for each stem length is analyzed. Here, S80A0 refers to a Boxfish model with an 80 mm stem length and a 0° attack angle. The positive value denotes an increase in the drag coefficient. On the other side, negative values indicate that the enlarged surface inspired by life has decreased the drag coefficient.

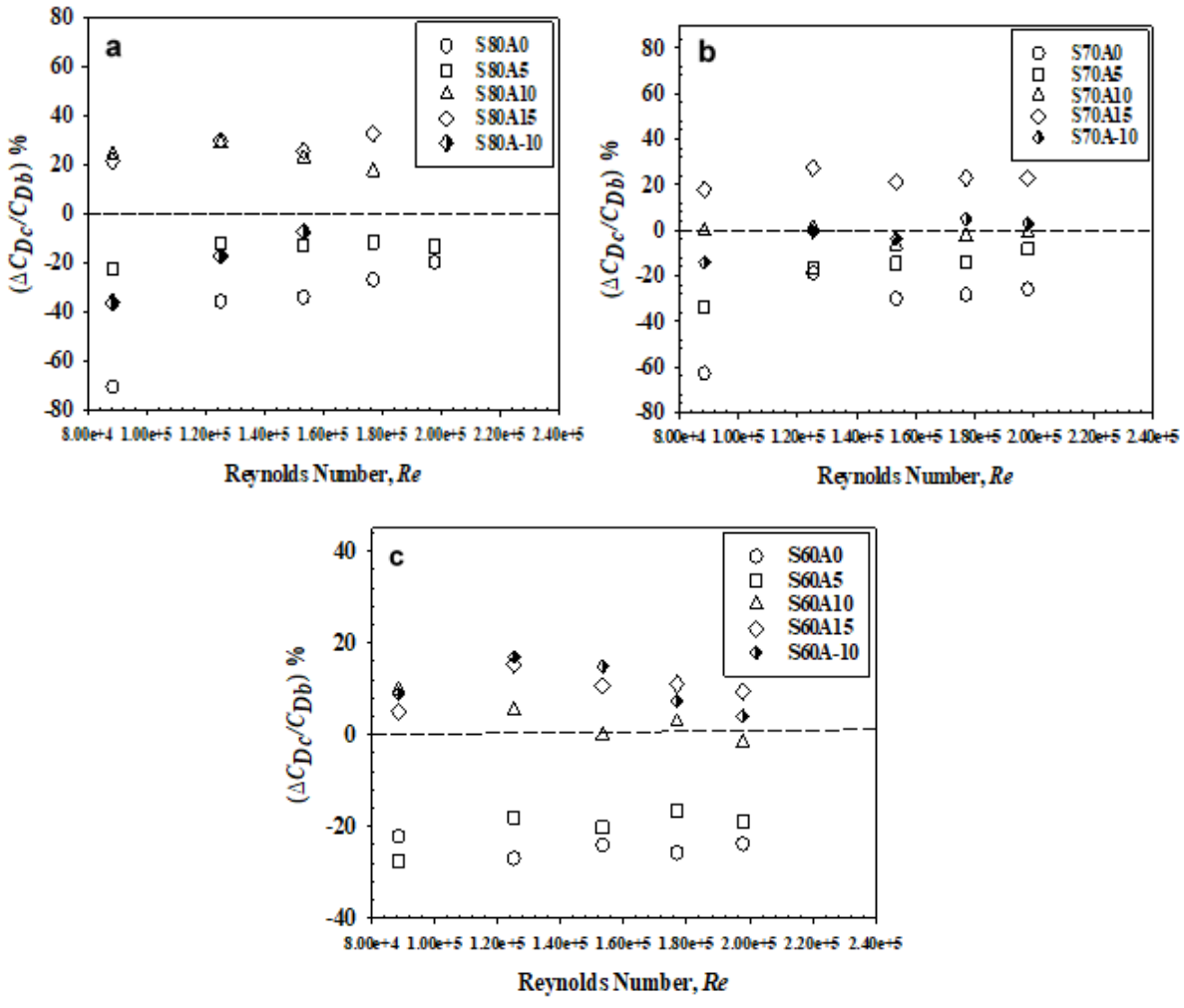

Figure 11: Experimental effectiveness of extended surface model with stem length (**a)** 80 mm; (**b)** 70 mm; and (**c)** 60 mm

Of the stem length variations represented in Figures 11a, b, and c, a stem of 80 mm with an attack angle of 0° exhibited the greatest reduction in drag, nearly 71%. In addition, the majority of drag reduction may be observed at 0° angles of attack in all testing circumstances. Owing to the Boxfish's aerodynamically efficient frontal shape and the extended surface's ability to effectively reduce drag induced by the interaction of separation flow between the extended surface and the cylinder. The boundary layer separation and reattachment take place at the extended surface and on the cylinder, especially downstream of the cylinder. Because the extended surface is in touch with the free stream flow at that point, drag is reduced. In addition, the separation of the boundary layer on the extended surface causes vortices to form between the gap (stem length) of the extended surface and the cylinder (Sohankar et al., 2019).

When the stem length lowers, the drag coefficient increases due to the Boxfish frontal shape's extended surface covering a significant portion of the cylinder and generating enormous air pockets that lead to substantial oscillatory vortex shedding. Huge air pockets considerably increase the cylinder's resistance to motion when there is a little gap between the expanded surface and the cylinder. When there is a large distance between the extended surface and the cylinder, however, the air pockets have time to contract and exert less drag on the circular cylinder. Unfortunately, as the angle of attack increases, the fluid cannot flow efficiently, particularly upstream and downstream of the cylinder, resulting in increased drag and unwanted vibration.

4.3 Numerical result

More computational fluid dynamics research is being done to investigate the flow properties of the extended surface. The numerical simulation considers three distinct Reynolds values in order to better comprehend the flow pattern and compare the experimental results to the simulation results. Table 1 compares the drag coefficients of three models with extended surfaces with Reynolds numbers of 8.85×10^4, 1.53×10^5, and 1.98×10^5 respectively. Two angles of attack are chosen based on the lowest drag at the lowest Reynolds number, and simulations are performed in that range. It is evident from Table 1 that the computed and measured C_D values for all examples are extremely close to the Reynolds number with the highest value. There are variations in C_D values for flows with a low Reynolds number, which may be the result of the transition from laminar to turbulent flow.

Table 1: Extended surface simulation of the Boxfish model

	S-80 mm				S-70 mm				S-60 mm			
Re	A-0		A-5		A-0		A-5		A-0		A-5	
	Exp	CFD	Exp	CFD	Exp	CFD	Exp	CFD	Exp	CFD	Exp	CFD
8.85×10^4	0.20	0.39	0.50	0.42	0.24	0.41	0.43	0.42	0.51	0.43	0.47	0.43
1.53×10^5	0.35	0.37	0.47	0.37	0.37	0.37	0.46	0.39	0.41	0.35	0.43	0.40
1.98×10^5	0.42	0.36	0.45	0.37	0.38	0.37	0.48	0.38	0.40	0.38	0.42	0.39

In addition to the comparison presented in the table above, the selected scenarios are elaborated upon to highlight the advantages of employing the extended surface. Consequently, the vortex behind a bare cylinder, a cylinder with an 80 mm stem, and a cylinder with a 70 mm stem are depicted in Figure 12 at $Re = 1.53\times10^5$.

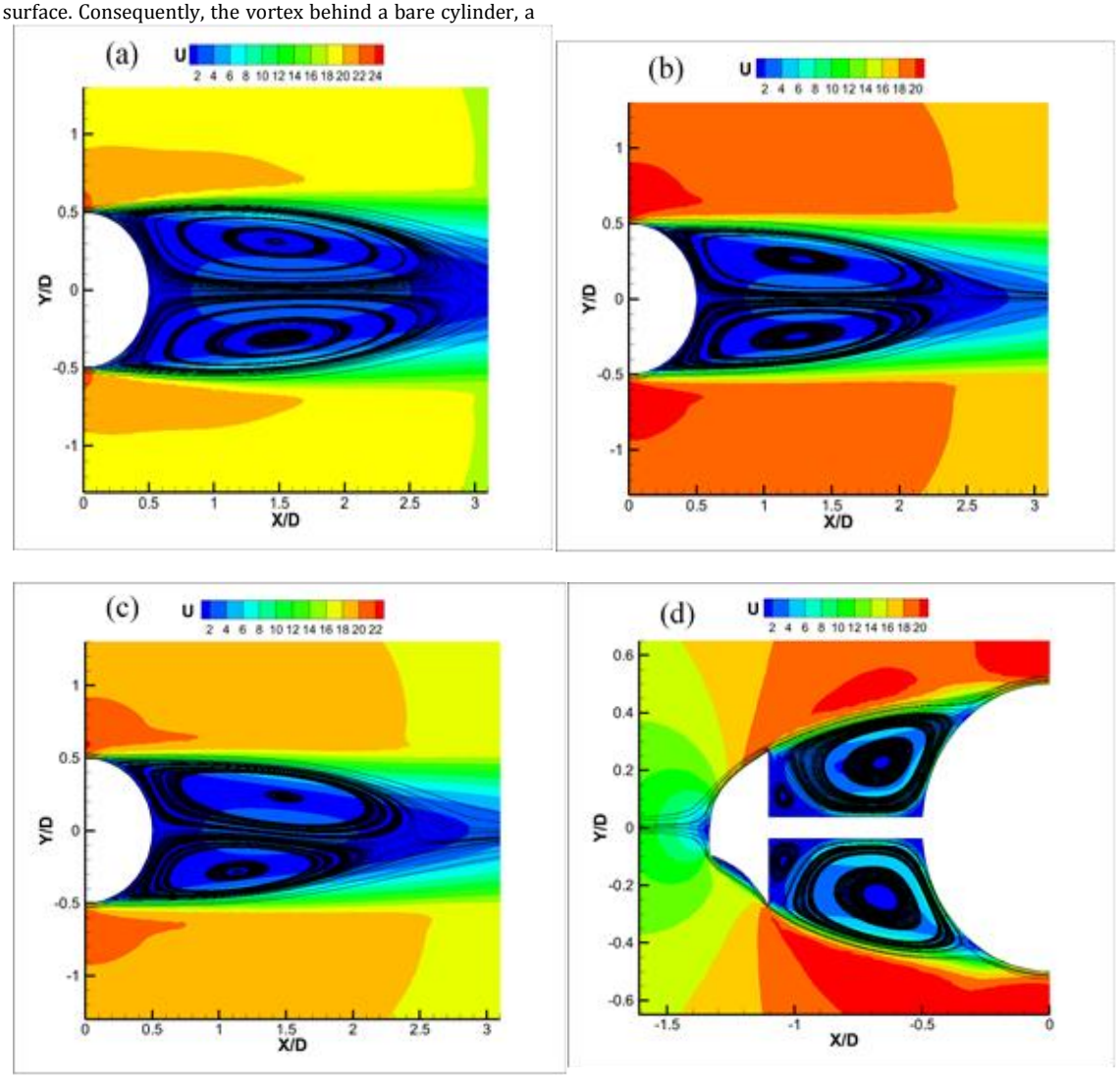

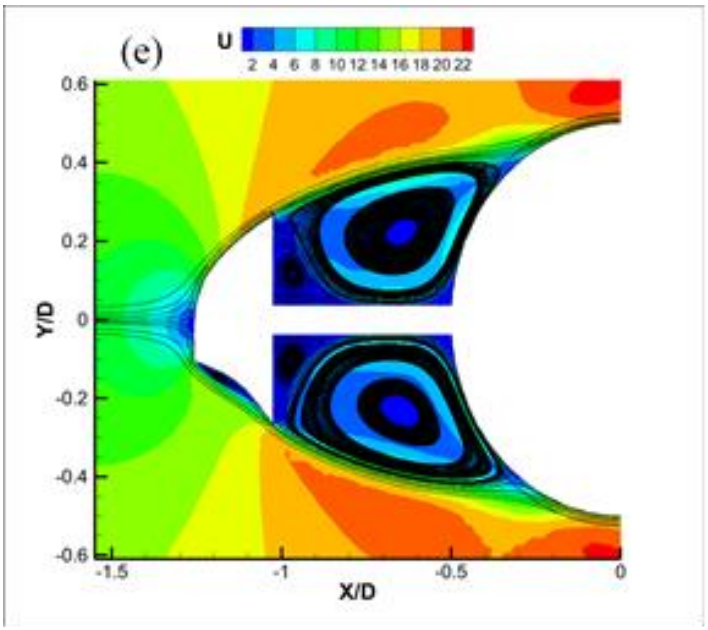

Figure 12: Velocity contour at *Re* = 1.53×10^5 with streamlines for behind (**a**) bare cylinder, cylinder with (**b**) 80 mm stem, (**c**) 70 mm stem, and in front of cylinder with (**d**) 80 mm stem, (**e**) 70 mm stem

Figure 12 depicts the vortex created behind a cylinder with a stem length of 80 mm and 70 mm for *Re* = 1.53×10^5, and compares it to a cylinder with no stem when the angle of attack (AOA) is set to 0. Both of these scenarios result in coefficients of drag that are substantially lower than those of the cylinder in its natural state. As shown in Figures 12a–c, the vortices are substantially extended along the flow direction behind the cylinder, resulting in a reduced drag coefficient. This is because the magnitude of the vortices has been drastically reduced. Figures 12d and 12e depict the flow patterns between the boxfish frontal shape and the cylinder in order to determine the effect of the stem length. For the 80 mm stem length, it is observed that the vortices, also known as quasi-steady vortices, for both the upper and lower portions, are significantly stretched along the flow direction at the downstream of the cylinder as compared with the bare cylinder (Alam et al., 2006). Therefore, the reattachment to the cylinder occurs at a greater angle and contributes to the shear layer, there by reducing pressure downstream of the cylinder (Alam et al., 2006). Additionally, based on the numerical streamlines, the produced air pockets or vortex pairs are extraordinarily large in between the extended surface and the cylinder. Therefore, the length of the stem or the space between the extended surface and the cylinder is one of the most influential factors for wake formation and, consequently, for drag reduction (Shoshe et al., 2021; Sohankar et al., 2019).

4.3.1 Velocity of Flow Field

Observations of velocity distributions at various downstream positions of the cylinder are made in order to determine the effect of the extended surface and stem length. As shown in Figure 13, four positions are chosen at X/D = 0.5, 1, 1.5, and 2.

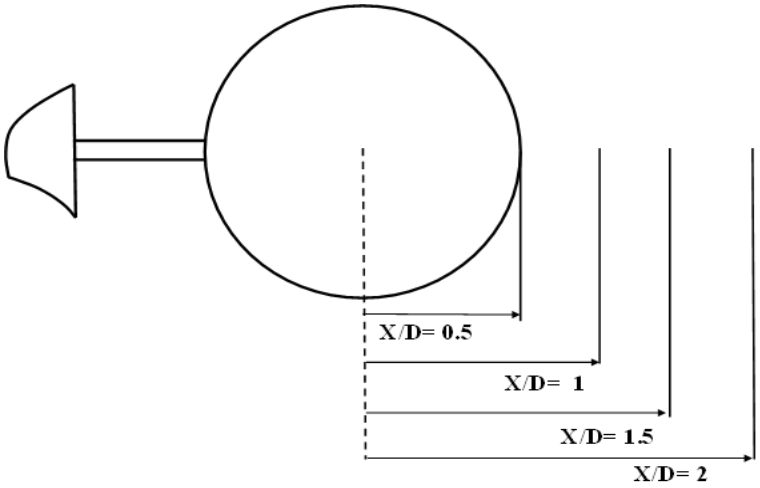

Figure 13: The layout of lines for velocity distribution

Figure 14 illustrates the velocity distribution (U/U_α) at various downstream positions for a number of cases. To be specific, for the *Re* = 8.85×10^4, the bare cylinder, the extended surface with the stem length of 80 mm for an angle of attack of 0^o (71% drag reduction), -10^o (36% drag reduction), and finally, for the *Re* = 1.25×10^4 while the angle of attack is 15^o (30% drag increased), are explicitly explaining to highlight the flow characteristics. Figure 14a shows the velocity distribution at *Re* = 8.85×10^4 for the bare cylinder and reveals that the flow patterns are symmetric with respect to the y-axis. X/D = 0.5 is distinct from the other positions because it is the closest to the cylinder and makes contact with it.

Alternatively, for the same Reynolds number, when the extended surfaces are placed in front of the cylinder, for instance, at 80 mm, the velocity profiles become asymmetric (Figures 14b) because of the asymmetric nature of the extended surface, and the velocities are significantly reduced in the y direction, particularly on the lower side of the cylinder. Several researches, such as reported that the tendencies of reducing the velocity in the flow direction and also in lateral directions ultimately cause a higher pressure behind the cylinder, resulting in a lower drag coefficient compared to the bare cylinder (Ji et al., 2023; Qi et al., 2022). Taking into account the variations in the angle of attack from -10^o to 15^o (Figures 14c and 14d) for Reynolds numbers of 8.85×10^4 and 1.25×10^5, respectively, and for the same stem length, the velocity is reduced in the y direction, thereby reducing the drag. However, the velocity distribution in Figure 14 d is much more covered in the y direction, resulting in a lower pressure distribution at downstream and hence a higher drag coefficient.

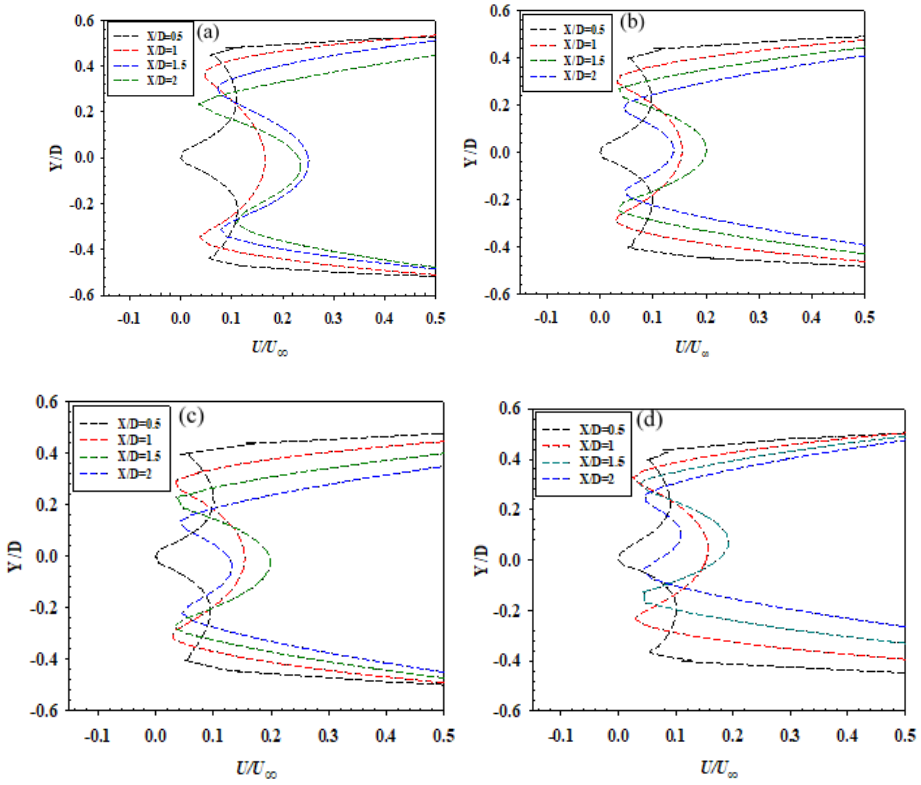

Figure 14: Velocity distribution behind circular cylinder under at different X/D conditions for *Re* = 8.85×10⁴ (a) bare cylinder, (b) 80 mm stem length, 80 mm stem length with angle of attack at (c) -10°, (d) 15° for *Re* = 8.85×10⁴ and *Re* = 1.25×10⁵ respectively

4.3.2 Turbulent Kinetic Energy

In turbulent flow, the turbulent eddies are associated with the turbulence kinetic energy (TKE). In principle, a higher value of TKE implies a more turbulent flow. The wake vortices are generated by the turbulent kinetic energy of the flow; as this energy decreases, so does the generation of the vortices, resulting in a higher energy flow recovery and a decrease in drag. Figure 15 depicts the TKE distributions behind the circular cylinder in various cases, as shown in Figure 14. The distribution pattern of the TKE for the bare cylinder is shown in Figure 15a, and the TKE is greater in downstream positions and is significantly higher at the vortex's periphery. As shown in Figure 15b, TKEs are reduced for the cylinder with the extended surface for a stem length of 80 mm. Due to the asymmetric nature of the frontal shape of the extended surface, it should be noted that the shear layer increases the TKE in the positive y direction and depicts a highly turbulent flow compared to the negative y direction. The lower values of TKE exhibit lesser turbulent flow for the cylinder with an extended surface and indicate that less flow energy is required for the formation of vortices behind the cylinder, particularly in the wake region. As a consequence, the drag force decreases. As shown in Figure 15c, the angle of attack has a significant effect on the occurrence of an asymmetric flow pattern, which is consistent with the observed results. It should be noted here that the maximum and minimum values of TKEs are increased as compared with the case shown in Figure 15b. These values are much higher for the lower X/D positions, especially in the vortex peripheral region, resulting in a lower reduction in drag coefficient. In Figure 15d, the TKE is significantly amplified as the Reynolds number and angle of attack increase, and hence the drag coefficient is much higher.

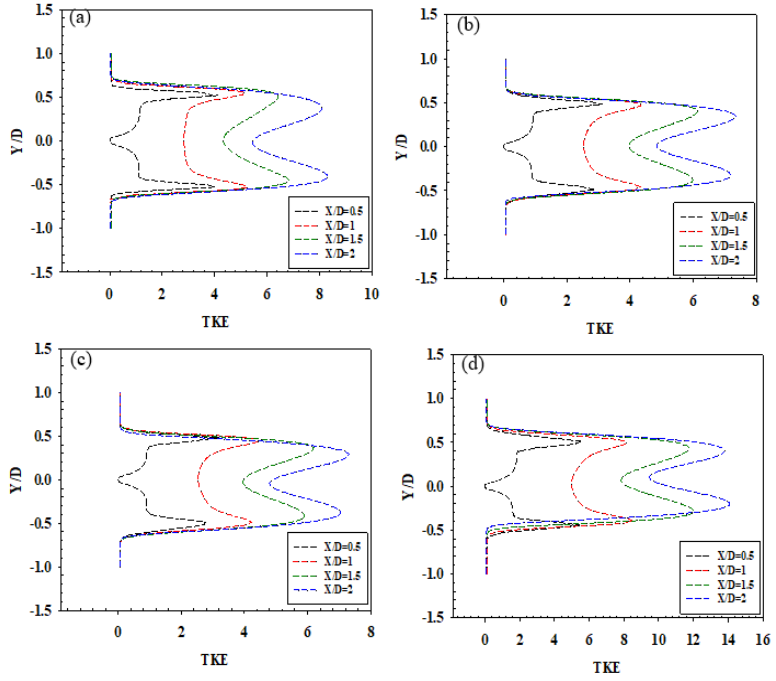

Figure 15: Turbulent Kinetic Energy (TKE) behind circular cylinder under at different X/D conditions for *Re* = 8.85×10⁴ (a) bare cylinder, (b) 80 mm stem length, 80 mm stem length with angle of attack at (c) -10°, (d) 15° for *Re* = 8.85×10⁴ and *Re* = 1.25×10⁵ respectively

5. Conclusion

Inspired by the Boxfish, a detailed study has been conducted to lower the coefficient of drag. Initially, an exact shape of the frontal portion of a Boxfish was designed for the extended surface, but a negative effect was found that meant the drag coefficient was much higher than the bare cylinder for a wide range of Reynolds numbers. Therefore, a modified extended surface is designed out of the frontal portion of the Boxfish. Consideration was given to three different stem lengths while including the modified frontal shape of the Boxfish as an extended surface of the cylinder. All cases are evaluated in a subsonic wind tunnel over a broad Reynolds number range. In addition, *2D* numerical simulations of circular cylinders with an expanded surface are performed for a wide range of Reynolds numbers, *Re* (8.85×10^4 to 1.98×10^5). Using the transition SST *k-ω* model, a numerical simulation for the subcritical Reynolds number region was conducted. In accordance with the experiments, numerical simulations of geometrical shapes on the extended surface are done with a wide range of angles of attack.

The simulation findings are compared to both numerical and experimental results found in the scientific literature. From the studies, it has been found that the upstream position of the extended surface and the angle of attack influence the drag coefficient significantly. Indeed, the drag coefficient is substantially lower in all circumstances with a low Reynolds number compared to the bare cylinder. In addition, the extended surface with the longer stem length can be treated positively as the drag coefficient is much reduced. At a Reynolds number of $Re = 8.85\times10^4$, the stem length of 80 mm achieves the greatest reduction in drag. Furthermore, increasing or decreasing the angle of attack from 0^o doesn't exhibit any significant improvement in the drag coefficient. The numerical drag coefficient results match the experimental results well for the extended surface cases, especially at high Reynolds numbers.

It is found that the modified shape of the Boxfish is effective in reducing drag, especially in the subcritical Reynolds number range. Therefore, the presented geometrical shapes can be incorporated into many aerodynamic applications, especially in the subcritical Reynolds number regions and leading to an eco-friendlier transportation system.

Acknowledgement

This work was supported by the Mechanical and Production Engineering Department (MPE) of Ahsanullah University of Science and Technology (AUST).

Ethical Approval

This declaration is not applicable to this study.

Declaration of Competing Interest

The authors declare that they have no known competing financial interests or personal relationships that could have appeared to influence the work reported in this paper.

Funding

Not Applicable

Data Availability

Data are available upon request.

References

Abdulbari, H.A., Yunus, R.M., Abdurahman, N.H., and Charles, A., 2013. Going against the flow—A review of non-additive means of drag reduction. J. Ind. Eng. Chem. 19, Pp. 27–36. https://doi.org/10.1016/j.jiec.2012.07.023.

Achenbach, E., 1971. Influence of surface roughness on the cross-flow around a circular cylinder. J. Fluid Mech. 46, Pp. 321–335. https://doi.org/10.1017/s0022112071000569.

Aghaee-Shalmani, Y., and Hakimzadeh, H., 2022. Large eddy simulation of flow around semi-conical piers vertically mounted on the bed. Environ. Fluid Mech. 22, Pp. 1211–1232. https://doi.org/10.1007/s10652-022-09886-x/metrics.

Ahmed, D.H., Haque, M.A., and Rauf, M.A., 2017. Investigation of Drag Coefficient at Subcritical and Critical Reynolds Number Region for Circular Cylinder with Helical Grooves. Int. J. Marit. Technol. 8, Pp. 25–33. https://doi.org/10.29252/ijmt.8.25.

Alam, M.M., and Zhou, Y., 2008. Strouhal numbers, forces and flow structures around two tandem cylinders of different diameters. J. Fluids Struct. 24, Pp. 505–526. https://doi.org/10.1016/j.jfluidstructs.2007.10.001.

Alam, M.M., Elhimer, M., Wang, L., Jacono, D. Lo, and Wong, C.W., 2018. Vortex shedding from tandem cylinders. Exp. Fluids 59, Pp. 1–17. https://doi.org/10.1007/s00348-018-2501-8/metrics.

Alam, M.M., Sakamoto, H., and Zhou, Y., 2006. Effect of a T-shaped plate on reduction in fluid forces on two tandem cylinders in a cross-flow. J. Wind Eng. Ind. Aerodyn. 94, Pp. 525–551. https://doi.org/10.1016/j.jweia.2006.01.018.

Alderton, D., 1967. Encyclopedia of Aquarium & pond fish. Dorling Kindersley Limited, Great Britain.

Anderson, J.D., 2011. Fundamentals of Aerodynamics SI. 6th ed. McGraw-Hill Education, New York.

Asif, M.A., Gupta, A., Das, Rana, M.D.J., and Ahmed, D.H., 2016. Investigation of drag reduction through a flapping mechanism on circular cylinder. AIP Conf. Proc. 1754, Pp. 1–5. https://doi.org/10.1063/1.4958374.

Bearman, P.W., and Harvey, J.K., 2012. Control of circular cylinder flow by the use of dimples. AIAA J. 31, Pp. 1753–1756. https://doi.org/10.2514/3.11844.

Carmo, B.S., Meneghini, J.R., and Sherwin, S.J., 2010. Secondary instabilities in the flow around two circular cylinders in tandem. J. Fluid Mech. 644, Pp. 395–431. https://doi.org/10.1017/s0022112009992473.

Cheney, J.A., Stevenson, J.P.J., Durston, N.E., Maeda, M., Song, J., Megson-Smith, D.A., Windsor, S.P., Usherwood, J.R., and Bomphrey, R.J., 2021. Raptor wing morphing with flight speed. J. R. Soc. Interface 18, Pp. 1–14 https://doi.org/10.1098/rsif.2021.0349.

Eun, L.C., Rafie, A.S.M., Wiriadidjaja, S., and Marzuki, O.F., 2018. An overview of passive and active drag reduction methods for bluff body of road vehicles. Int. J. Eng. Technol. 7, Pp. 53–56. https://doi.org/10.14419/ijet.v7i4.13.21328.

García, P.M., and Vakkilainen, E., 2019. A comparison of turbulence models and two and three dimensional meshes for unsteady CFD ash deposition tools. Fuel, 237, Pp. 806–811. https://doi.org/10.1016/j.fuel.2018.10.066.

Ghosh, A., 2021. Metaheuristic optimization framework for drag reduction using bioinspired surface riblets. ArXiv 2, Pp. 1–7 https://doi.org/https://doi.org/10.48550/arxiv.2109.09650.

Gnatowska, R., 2019. Wind-induced pressure loads on buildings in tandem arrangement in urban environment. Environ. Fluid Mech. 19, Pp. 699–718. https://doi.org/10.1007/s10652-018-9646-0/figures/13.

Haidary, F.M., Mazumder, A., Hasan, M.R., Shoshe, M.A.M.S., and Ahmed, D.H., 2020. Investigation for the drag reduction by introducing a passage through a circular cylinder. Ann. Eng. 1, Pp. 1–13.

Han, X., Wang, J., Zhou, B., Zhang, G., and Tan, S.K., 2019. Numerical Simulation of Flow Control around a Circular Cylinder by Installing a Wedge-Shaped Device Upstream. J. Mar. Sci. Eng. 7, Pp. 422. https://doi.org/10.3390/jmse7120422.

Hoener, S.F., 1965. Pressure Drag.Pages 5–8 in Fluid Dynsmic Drag. 2nd ed. Hoener Fluid Dynamics, New York, United States.

Hojo, T., 2015. Control of flow around a circular cylinder using a patterned surface.Pages 245–256 in Computational Methods and Experimental Measurements XVII. Carlomagno, G.M., Poljak, D., Brebbia, and C.A., eds. WIT Press.

Holman, J.P., 2011. Analysis of Experimental Data.Pages 60–165 in Experimental Methods for Engineers. Lange, M., Stenquist, B., Buczek, L., eds. 8th ed. McGraw-Hill, New York.

Hucho, W.H., and Sovran, G., 1993. Aerodynamics of road vehicles. Annu. Rev. Fluid Mech 25, Pp. 485–537.

Igarashi, T., 1981. Characteristics of the Flow around Two Circular Cylinders Arranged in Tandem : 1st Report. Bull. JSME 24, Pp. 323–331. https://doi.org/10.1299/jsme1958.24.323.

Islam, A., Shoshe, M.A.M.S., and Ahmed, D.H., 2023. Reduction of Total Drag for Finite Cylinders in Turbulent Flow with a Half-C Shape Upstream Body. Int. J. Fluid Mech. Res. 50, Pp. 41–53. https://doi.org/10.1615/interjfluidmechres.2022045488.

Ji, L., Du, H., Yang, L.J., Zhang, W.X., Chen, S., and Zhang, Q.L., 2023. Research on the drag reduction characteristics and mechanism of a cylinder covered with porous media. AIP Adv. 13, Pp. 035220. https://doi.org/10.1063/5.0141832/2881255.

Kerho, M.F., Held, J.P., Kramer, B.R., and Ng, T., 2000. Active drag reduction using selective low rate suction.in 18th Applied Aerodynamics Conference. Denver,CO,U.S.A.

Korycki, M., Łobocki, L., and Wyszogrodzki, A., 2016. Numerical simulation of stratified flow around a tall building of a complex shape. Environ. Fluid Mech. 16, Pp. 1143–1171. https://doi.org/10.1007/s10652-016-9470-3/figures/14.

Kozlov, A., Chowdhury, H., Mustary, I., Loganathan, B., and Alam, F., 2015. Bio-Inspired Design: Aerodynamics of Boxfish. Procedia Eng. 105, Pp. 323–328. https://doi.org/10.1016/j.proeng.2015.05.007.

Law, Y.Z., and Jaiman, R.K., 2017. Wake stabilization mechanism of low-drag suppression devices for vortex-induced vibration. J. Fluids Struct. 70, Pp. 428–449. https://doi.org/10.1016/j.jfluidstructs.2017.02.005.

Liess, H.D., and Ilgevičius, A., 2003. Analytical versus numerical calculations of physical problems. The benefits of its combination. Math. Model. Anal. 8, Pp. 291–302. https://doi.org/10.1080/13926292.2003.9637231.

Lin, J.C., Yang, Y., and Rockwell, D., 2002. Flow past two cylinders in tandem: instantaneous and averaged flow structure. J. Fluids Struct. 16, Pp. 1059–1071. https://doi.org/10.1006/jfls.2002.0469.

Malan, P., Suluksna, K., and Juntasaro, E., 2022. Calibrating the γ-Reθ transition model for commercial CFD.Pages 1–20 in 47th AIAA Aerospace Sciences Meeting including the New Horizons Forum and Aerospace Exposition. Orlando.

Matsuura, K., 2015. Taxonomy and systematics of tetraodontiform fishes: a review focusing primarily on progress in the period from 1980 to 2014. Ichthyol. Res. 62, Pp. 72–113. https://doi.org/10.1007/s10228-014-0444-5.

Menter, F.R., 1993. Improved Two-Equation κ-ω Turbulence Models for Aerodynamic Flows. AIAA 23rd Fluid Dyn. Plasmadynamics, Lasers Conf., Pp. 1–38. https://doi.org/10.2514/6.1993-2906.

Menter, F.R., Langtry, R.B., Likki, S.R., Suzen, Y.B., Huang, P.G., and Völker, S., 2006. A correlation-based transition model using local variables - Part I: Model formulation. J. Turbomach., 128, Pp. 413–422. https://doi.org/10.1115/1.2184352.

Munson, B.R., Young, D.F., and Okiishi, T.H., 1998. Fundamentals of fluid mechanics. Wiley.

Nazari, S., Zamani, M., and Moshizi, S.A., 2018. Comparison between two-dimensional and three-dimensional computational fluid dynamics techniques for two straight-bladed vertical-axis wind turbines in inline arrangement. Wind Eng. 42, Pp. 647–664. https://doi.org/10.1177/0309524x18780384.

Nethercot, D.A., 2002. The importance of combining experimental and numerical study in advancing structural engineering understanding. J. Constr. Steel Res. 58, Pp. 1283–1296. https://doi.org/10.1016/s0143-974x(02)00011-1.

Oanta, E., Raicu, A., and Menabil, B., 2020. Applications of the numerical methods in mechanical engineering experimental studies. IOP Conf. Ser. Mater. Sci. Eng., 916, Pp. 012074 https://doi.org/10.1088/1757-899x/916/1/012074.

Prasad, A., and Williamson, C.H.K., 1997. A method for the reduction of bluff body drag. J. Wind Eng. Ind. Aerodyn. 69, Pp. 155–167. https://doi.org/10.1016/s0167-6105(97)00151-7.

Qi, J., Qi, Y., Chen, Q., and Yan, F., 2022. A study of drag reduction on cylinders with different v-groove depths on the surface. Water (Switzerland) 14 https://doi.org/10.3390/w14010036.

Rosetti, G.F., Vaz, G., and Fujarra, A.L.C., 2012. URANS calculations for smooth circular cylinder flow in a wide range of reynolds numbers: Solution verification and validation. J. Fluids Eng. Trans. ASME, 134, Pp. 1–18. https://doi.org/10.1115/1.4007571.

Saleh, Z.M., Student, M.S., Ali, A.H., and Abood, M.S., 2020. Drag Reduction Using Passive Methods on KIA PRIDE Car Model. J. Eng. 26, Pp. 47–63. https://doi.org/10.31026/j.eng.2020.04.04.

Savill, A.M., 1990. Drag Reduction by Passive Devices—a Review of some Recent Developments. Struct. Turbul. Drag Reduct., Pp. 429–465. https://doi.org/10.1007/978-3-642-50971-1_36.

Selig, M.S., 2003. Low Reynolds Number Airfoil Design Lecture Notes. , Pp. 1–43.

Shoshe, M.A.M.S., Islam, A., and Ahmed, D.H., 2021. Effect of an upstream extended surface on reduction of total drag for finite cylinders in turbulent flow. Int. J. Fluid Mech. Res. 48, Pp. 27–44. https://doi.org/10.1615/interjfluidmechres.2021038255.

Siddiqui, N.A., and Agelin-Chaab, M., 2021. Nature-inspired solutions to bluff body aerodynamic problems: A review. J. Mech. Eng. Sci. 15, Pp. 1–52. https://doi.org/10.15282/jmes.15.2.2021.13.0638.

Sohankar, A., Khodadadi, M., Rangraz, E., and Alam, M.M., 2019. Control of flow and heat transfer over two inline square cylinders. Phys. Fluids 31, Pp. 12–36. https://doi.org/10.1063/1.5128751.

Sowoud, K.M., Al-Filfily, A.A., and Abed, B.H., 2020. Numerical Investigation of 2D Turbulent Flow past a Circular Cylinder at Lower Subcritical Reynolds Number. IOP Conf. Ser. Mater. Sci. Eng. 881, Pp. 1–12. https://doi.org/10.1088/1757-899x/881/1/012160.

Stringer, R.M., Zang, J., and Hillis, A.J., 2014. Unsteady RANS computations of flow around a circular cylinder for a wide range of Reynolds numbers. Ocean Eng. 87, Pp. 1–9. https://doi.org/10.1016/j.oceaneng.2014.04.017.

Sudin, M.N., Abdullah, M., Ramli, F., Musthafah, M.T., and Shamsudin, S.A., 2014. Review of Research on Vehicles Aerodynamic Drag Reduction Methods. Int. J. Mech. Mechatronics Eng. 14, Pp. 35–47.

Tsutsui, T., and Igarashi, T., 2002. Drag reduction of a circular cylinder in an air-stream. J. Wind Eng. Ind. Aerodyn. 90, Pp. 527–541. https://doi.org/10.1016/s0167-6105(01)00199-4.

Wang, L., Mahbub Alam, M., and Zhou, Y., 2018. Two tandem cylinders of different diameters in cross-flow: effect of an upstream cylinder on wake dynamics. J. Fluid Mech., 836, Pp. 5–42. https://doi.org/10.1017/jfm.2017.735.

Wu, J., Welch, L.W., Welsh, M.C., Sheridan, J., and Walker, G.J., 1994. Spanwise wake structures of a circular cylinder and two circular cylinders in tandem. Exp. Therm. Fluid Sci. 9, Pp. 299–308. https://doi.org/10.1016/0894-1777(94)90032-9.

Xu, G., and Zhou, Y., 2004. Strouhal numbers in the wake of two inline cylinders. Exp. Fluids 37, Pp. 248–256. https://doi.org/10.1007/s00348-004-0808-0/metrics.

Yuce, M.I., and Kareem, D.A., 2016. A numerical analysis of fluid flow around circular and square cylinders. J. Am. Water Works Assoc. 108, Pp. 546–554. https://doi.org/10.5942/jawwa.2016.108.0141.

Zdravkovich, M.M., 1990. Conceptual overview of laminar and turbulent flows past smooth and rough circular cylinders. J. Wind Eng. Ind. Aerodyn. 33, Pp. 53–62. https://doi.org/10.1016/0167-6105(90)90020-d.

Zhang, L., Shan, X., and Xie, T., 2020. Active Control for Wall Drag Reduction: Methods, Mechanisms and Performance. IEEE Access 8, Pp. 7039–7057. https://doi.org/10.1109/access.2020.2963843.

Zhang, P.F., Wang, J.J., and Huang, L.X., 2006. Numerical simulation of flow around cylinder with an upstream rod in tandem at low Reynolds numbers. Appl. Ocean Res. 28, Pp. 183–192. https://doi.org/10.1016/j.apor.2006.08.003.